

Ordered Vacancy Compound Formation at the Interface of Cu(In,Ga)Se₂ Absorber with Sputtered In₂S₃-Based Buffers: An Atomic-Scale Perspective

Oana Cojocaru-Mirédin,* Dimitrios Hariskos, Wolfram Hempel, Ana Kanevce, Xiaowei Jin, Jens Keutgen, Mohit Raghuvanshi, Reinhard Schneider, Roland Scheer, Dagmar Gerthsen, and Wolfram Witte


The design of a Cd-free and wider-bandgap buffer layer is stringent for future Cu(In,Ga)Se₂ (CIGSe) thin-film solar cell applications. For that, an In₂S₃ buffer layer alloyed with a limited amount of O (well below 25 mol%) has been proposed as a pertinent alternative solution to CdS or Zn(O,S) buffers. However, the chemical stability of the In₂S₃/CIGSe heterointerface when O is added is not completely clear. Therefore, in this work, the buffer/absorber interface for a series of sputter-deposited In₂S₃ buffers with and without O is investigated. It is found that the solar cell with the highest open-circuit voltage is obtained for the O-free In₂S₃ buffer sputtered at 220 °C. This improved open-circuit voltage could be explained by the presence of a 20 nm-thick ordered vacancy compound (OVC) at the absorber surface. A much thinner OVC layer (5 nm) or even the absence of this layer is found for the cell with In₂(O_{0.25}S_{0.75})₃ buffer layer where O is inserted. The volume fraction of the OVC layer is directly linked with the magnitude of Cu diffusion from the CIGSe surface into the In₂(O_xS_{1-x})₃ buffer layer. The O addition strongly reduces the Cu diffusion inside the buffer layer up to complete suppression for very high O contents in the buffer. Finally, it is discussed that the presence of the OVC layer may lower the valence band maximum, thereby forming a hole barrier, suppressing charge carrier recombination at the In₂(O_xS_{1-x})₃/CIGSe interface, which could result in an increased open-circuit voltage.

1. Introduction

Cadmium sulfide (CdS) is a direct-bandgap semiconductor, which has been widely used as a buffer in thin-film solar cells applications. This is because of its outstanding properties such as low resistivity, high optical transparency, excellent thermal stability, and low costs.^[1–3] However, this buffer raises some concerns such as: 1) parasitic absorption in the short-wavelength region (i.e., in the UV); 2) toxicity of the Cd element which can pollute the environment and harm human health; 3) deposition technique which is typically a wet chemical process, so-called chemical bath deposition (CBD), requiring breaking the vacuum during an industrial in-line CIGS module processing including a roll-to-roll process on flexible substrates; and finally 4) the management of the wet chemical waste (final deposit or recycling). More specifically, the in situ in-line process developed for the absorber layer Cu(In,Ga)Se₂ (CIGSe) deposition as well as i-ZnO and ZnO:Al top contact sputtering

O. Cojocaru-Mirédin
INATECH
University of Freiburg
Emmy-Noether-Straße 2, 79110 Freiburg im Breisgau, Germany
E-mail: oana.cojocaru-miredin@inatech.uni-freiburg.de

O. Cojocaru-Mirédin, J. Keutgen, M. Raghuvanshi
I. Institute of Physics
RWTH Aachen University
Sommerfeldstraße 14, 52074 Aachen, Germany

 The ORCID identification number(s) for the author(s) of this article can be found under <https://doi.org/10.1002/solr.202400574>.

© 2024 The Author(s). Solar RRL published by Wiley-VCH GmbH. This is an open access article under the terms of the Creative Commons Attribution-NonCommercial-NoDerivs License, which permits use and distribution in any medium, provided the original work is properly cited, the use is non-commercial and no modifications or adaptations are made.

DOI: 10.1002/solr.202400574

D. Hariskos, W. Hempel, A. Kanevce, W. Witte
Zentrum für Sonnenenergie- und Wasserstoff-Forschung Baden-Württemberg (ZSW)
Meitnerstraße 1, 70563 Stuttgart, Germany

X. Jin, M. Raghuvanshi
Fraunhofer-Institut für Angewandte Festkörperphysik IAF
Tullastraße 72, 79108 Freiburg, Germany

R. Schneider
Laboratory for Electron Microscopy (LEM)
Karlsruhe Institute of Technology (KIT)
Engesserstraße 7, 76131 Karlsruhe, Germany

R. Scheer, D. Gerthsen
Institut für Physik
FG Photovoltaik
Martin Luther-Universität Halle-Wittenberg
von-Danckelmann-Platz 3, 06099 Halle, Germany

needs to be interrupted to perform the CBD process for the thin CdS layer growth. Therefore, having a sputtered Cd-free buffer layer that can be easily integrated without vacuum breaks in a full-stack deposition process is highly desired for the advancement of the CIGSe thin-film technology.

Several alternative Cd-free buffer layers have already been proposed such as In_2S_3 ,^[4-7] ZnS ,^[8,9] $\text{Zn}(\text{O},\text{S})$,^[10,11] $\text{Zn}_x\text{Ti}_y\text{O}$,^[12] $\text{Zn}_{1-x}\text{Sn}_x\text{O}_y$,^[13] $\text{Zn}_{1-x}\text{Mg}_x\text{O}$,^[14] $\text{In}_x(\text{O},\text{OH},\text{S})_y$,^[15] $\text{Zn}(\text{O},\text{S},\text{OH})_x$,^[16,17] $\text{Sn}_{1-x}\text{Ge}_x\text{O}_y$, $\text{Zn}_{1-x}\text{Ge}_x\text{O}_y$,^[18] and $\text{Sn}_{1-x}\text{Ga}_x\text{O}_y$.^[19] In this work, we are going to focus on the In_2S_3 -based buffer layers. The stoichiometric In_2S_3 compound has an indirect bandgap of about 2.1 eV^[20,21] depending on the deposition methods employed, very close to the one of 2.4 eV measured for CdS. Yet, such low-bandgap values for the buffer have been proven to induce some optical absorption loss at wavelengths below ≈ 550 nm reducing the quantum efficiency in the blue-wavelength region of the solar spectrum.^[22] Therefore, it is suggested that the buffer layers should be based on wider-bandgap semiconductors. A very promising way of enlarging the bandgap is to alloy the buffer with O. A notable example is given for CdS where the presence of O has not only drastically increased the bandgap value, but also has maximized the device performance.^[22] He et al.^[22] have shown that the 26 nm Cu depletion and the Cd counterdoping below the CIGSe surface are responsible for this efficiency increase. Yet, the CIGSe cell with the highest O content in CdS buffer exhibits the lowest efficiency, proving that too much O in the buffer layer is detrimental. Interestingly, O addition into a ZnS buffer (bandgap 3.6 eV) results in a strong bowing with minimum values down to 2.6 eV increasing to values up to 3.2 eV for pure ZnO,^[23] which is larger compared to CdS (≈ 2.4 eV). This reduced absorption leads to an increase in the short-circuit current density (J_{sc}) because more blue light reaches the CIGSe absorber layer.

Several research works have performed alloying the In_2S_3 with O.^[15,24-27] The $\text{In}_x(\text{O},\text{OH},\text{S})_y$ buffer is a mixture of In_2S_3 and $\text{In}_2\text{O}_3/\text{In}(\text{OH})_3$ phases where the In_2S_3 has an indirect low bandgap of 2.1 eV, while the $\text{In}_2\text{O}_3/\text{In}(\text{OH})_3$ phase has a direct bandgap of 3.5 eV.^[15] Therefore, it has been suggested that increasing the O content in the $\text{In}_x(\text{O},\text{OH},\text{S})_y$ buffer will help in increasing the overall bandgap value. However, the same work^[15] showed that the cells containing higher O content in the $\text{In}_x(\text{O},\text{OH},\text{S})_y$ buffer exhibit lower efficiencies. This finding is in agreement with the recent work of Ghorbani et al.^[25] implying that O, when incorporated in too high concentrations, becomes lethal to the cells. This detrimental effect of O (when found in too high concentrations) has been explained by the increase of the non-favorable band offset between the CIGSe absorber and the $\text{In}_2(\text{O}_x\text{S}_{1-x})_3$ buffer as calculated by density functional theory resulting in a pronounced degradation of the open-circuit voltage (V_{OC}).^[25]

With these works, it becomes clear that a high O content in the In_2S_3 buffer is detrimental to the cell performance, but not much is clarified when O is present in low quantities, especially at the $\text{In}_2(\text{O}_x\text{S}_{1-x})_3/\text{CIGSe}$ heterointerface. Moreover, it has been proved several times that deposition of In_2S_3 buffer layer on the CIGSe absorber at temperatures above 200 °C leads to the formation of ordered vacancy compounds (OVCs) at the CIGSe surface.^[28,29] However, it is not known if this OVC phase still forms when In_2S_3 buffer layer is alloyed with O.

Therefore, in this work, we are going to focus on the effect of moderate O concentration on the electrical, structural, and chemical properties of the buffer/absorber interface. This will be realized using electron beam-induced current (EBIC) in combination with high-resolution nanoanalytical techniques such as atom probe tomography (APT) and high-resolution transmission electron microscopy (HRTEM) in the micrometer range.

2. Results and Discussions

2.1. Parameters of CIGSe Solar Cells Containing Sputtered In_2S_3 and $\text{In}_2(\text{O},\text{S})_3$ Buffers

Figure 1a,b provides the efficiency and V_{OC} values obtained for CIGSe cells with the standard CdS buffer layer as well as the sputtered In_2S_3 and $\text{In}_2(\text{O}_{0.25}\text{S}_{0.75})_3$ buffer layers within our experimental campaign. The corresponding J - V curves of representative cells are depicted in Figure S1, Supporting Information with its corresponding solar cell parameters listed in Table S1, Supporting Information. While the efficiency for the cells with the sputtered pure In_2S_3 buffer layer is much lower than the cell with the CdS buffer, we observe however that the efficiency can be significantly improved by applying a higher deposition temperature of 220 °C and by adding a reduced amount of oxygen to In_2S_3 . The sputter deposition of In_2S_3 buffer layer at 220 °C leads indeed to a strong improvement of the V_{OC} (Figure 1b) and some increase in J_{sc} (Table S1, Supporting Information). The addition of oxygen instead leads to a slightly lower V_{OC} compared with the pure In_2S_3 deposited at 220 °C.

We often observed higher J_{sc} values for CIGSe solar cells with thin In_2S_3 -based buffers with thicknesses around 30 nm compared to reference cells with 50 nm-thick CdS buffer due to reduced parasitic absorption in the short-wavelength region between 350 and 550 nm.^[30] Nevertheless, we always observed lower efficiencies for CIGSe cells with In_2S_3 -based buffer layers compared to CdS-buffered reference cells, mainly due to reduced V_{OC} and fill factor (FF) values. This trend is even more pronounced for cells with In_2S_3 -based buffers sputtered at room temperature (RT).^[25,31] Different rinsing procedures of the CIGSe surface and a post-annealing procedure of the complete cell stack can enhance these parameters.^[30] Besides the CIGSe surface conditioning and sputter parameters, especially the substrate temperature during buffer deposition, the chemical composition, for example, $[\text{Cu}]/([\text{Ga}]+[\text{In}])$ ratio of the CIGSe absorber may play an important role.

To deduce the dominating recombination mechanism of the cells under investigation, temperature-dependent V_{OC} values were extrapolated to 0 K for the J - V - T measurements presented in Figure 1c. The extracted activation energies E_a for the reference cell with the CdS buffer and the cells with rf- In_2S_3 @ 220 °C (rf- radio frequency sputtering) are in the range of the bandgap energy (which does not exclude entirely the interface recombination^[32,33]). For the sample rf- $\text{In}_2(\text{O}_{0.25}\text{S}_{0.75})_3$ @ 220 °C we observe already a slight decrease in the activation energy whereas the E_a for the rf- In_2S_3 @ RT cell is only 0.9 eV, which is well below the bandgap energy. This observation indicates that interface recombination is a dominant loss mechanism in the latter sample.

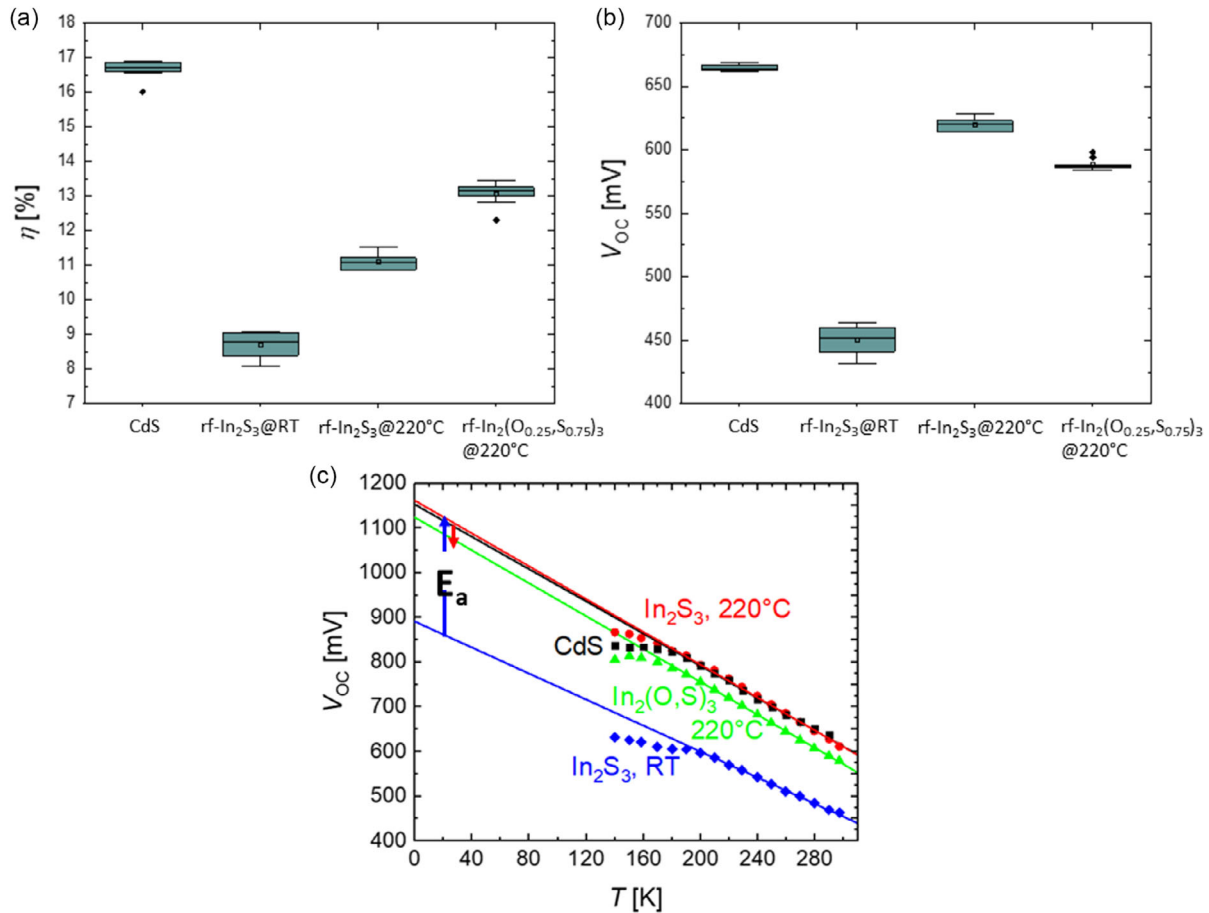


Figure 1. The a) power conversion efficiency (η) and b) open-circuit voltage (V_{OC}) for the CIGSe cells containing the standard CdS buffer layer as well as the sputtered In_2S_3 and $\text{In}_2(\text{O}_{0.25}\text{S}_{0.75})_3$ buffer layers. c) J - V - T measurement and extrapolation of V_{OC} to 0 K for representative CIGSe solar cells with In_2S_3 -based buffers and the CdS-buffered reference cell.

2.2. Properties of the Sputtered In_2S_3 and $\text{In}_2(\text{O},\text{S})_3$ Buffer Layers

The O addition to the In_2S_3 buffer results only in a minor change in stoichiometry. The buffer composition values obtained from the APT analyses are shown in **Table 1**. We could indeed clearly identify the 40:60 buffer stoichiometry in all three samples with $(\text{In},\text{Cu},\text{Na})_2(\text{O},\text{S})_3$. The presence of O in the buffer of the $\text{rf-In}_2(\text{O}_{0.25}\text{S}_{0.75})_3$ @ 220 °C sample has no impact on the buffer stoichiometry, but only that the increase in O content is compensated by the reduction in S content.

We find that the Cu and Se diffusion into the In_2S_3 -based buffer layer is reduced when O is present (see Table 1). First, for the pure In_2S_3 buffer, the Cu and Na contents both increase upon heat treatment with ≈ 1.4 and 0.08 at%, respectively. Probably the presence of the grain boundaries accelerates the diffusion of Cu and Na from the absorber into the buffer layer. Second, the presence of O inside the In_2S_3 buffer leads to a strong increase in the Na content (with about 0.9 at%) suggesting a certain affinity between the Na and O as claimed by Kronik et al.^[34] Yet, the Cu content decreased by 1.5 at% in the $\text{In}_2(\text{O}_{0.25}\text{S}_{0.75})_3$ layer suggests that the O presence reduces

Table 1. Buffer composition evaluated from the APT analyses. The values are averaged over four complete APT analyses on different locations for each sample. The statistical standard deviation is provided for each value.

Sample	Buffer composition					
	In [at%]	S [at%]	O [at%]	Cu [at%]	Na [at%]	Se [at%]
rf- In_2S_3 @ RT	38.2 ± 0.4	57 ± 0.5	0.26 ± 0.004	3 ± 0.04	0.17 ± 0.004	1.25 ± 0.01
rf- In_2S_3 @ 220 °C	36.2 ± 0.3	58 ± 0.6	0.2 ± 0.004	4.4 ± 0.05	0.25 ± 0.004	0.8 ± 0.01
rf- $\text{In}_2(\text{O}_{0.25}\text{S}_{0.75})_3$ @ 220 °C	37.3 ± 0.2	50 ± 0.2	8.2 ± 0.01	2.9 ± 0.1	1.1 ± 0.04	0.5 ± 0.01

the Cu diffusion inside the $\text{In}_2(\text{O}_{0.25}\text{S}_{0.75})_3$ buffer. The same applies also to Se. In fact, even if the Se content is lower than the one of Cu in the $\text{In}_2(\text{O}_{0.25}\text{S}_{0.75})_3$ buffer, the magnitude in Se and Cu reduction is quite similar (37% reduction in Se, which is very close to the 34% reduction in Cu).

It is worthwhile to note here that the stronger Cu diffusion into the In_2S_3 buffer when compared with $\text{In}_2(\text{O}_{0.25}\text{S}_{0.75})_3$ may also be related to the higher affinity of Cu to bond with S atoms than with O.^[35] Therefore, there seems to be a correlation between the amount of Cu and the particular S content of the $\text{In}_2(\text{O}_x\text{S}_{1-x})_3$ layer. For this reason, the Cu content is highest for In_2S_3 and appears to decrease with increasing O content of the buffer layers.

2.3. Cu and Na Diffusion Inside the $\text{In}_2(\text{O},\text{S})_3$ Buffer Layers

Although the Cu diffusion inside In_2S_3 at temperatures above 200 °C has been already reported,^[36] it is however not clear which impact O has on Cu diffusion. Moreover, the impact of Na on Cu diffusion was in the past ignored due to their difficulty in being analyzed, especially when found in such a low quantity. Therefore, model samples consisting of 200 nm-thick Cu_2Se deposited by sputtering on either rf-sputtered $\text{In}_2(\text{O}_x\text{S}_{1-x})_3$ (with $x = 0, 0.25, 0.5, 0.75,$ and 1) or rf-sputtered In_2S_3 : X mol% NaF layers (with $X = 0, 2,$ and 10 mol% NaF) have been synthesized to study Cu diffusion in rf- In_2S_3 containing either O or Na. These model samples with stacking sequence substrate/ In_2S_3 -based layers/ Cu_2Se (from bottom to top) were subsequently annealed at 220 °C for 30 min (i.e., the same temperature used during sputtering of the $\text{In}_2(\text{O},\text{S})_3$ -based buffers for the solar cell fabrication) to study the Cu diffusion into the In_2S_3 -containing layers influenced either by O or Na.

The time-of-flight secondary-ion mass spectrometry (ToF-SIMS) depth profiles after annealing the $\text{Cu}_2\text{Se}-\text{In}_2(\text{O},\text{S})_3$ model samples at 220 °C for 30 min revealed that the presence of O in $\text{In}_2(\text{O},\text{S})_3$ blocks the Cu diffusion from Cu_2Se into the $\text{In}_2(\text{O},\text{S})_3$ -based layers (see Figure 2a), while the presence of Na has no or minor impact on Cu diffusion (see Figure 2b). It should be noted that the Cu diffusion into pure In_2S_3 is the same for the In_2S_3 films deposited at RT and 220 °C, most probably due to their crystalline structure.^[28] The results on the model samples validate the APT findings on complete solar cells described above, where the Cu content inside the In_2S_3 buffer is reduced when O is present. The Na presence in In_2S_3 buffer seems to have no or minor impact on Cu diffusion inside In_2S_3 . Yet, the Na content in Table 1 strongly increases when O is present in the buffer, suggesting a strong Na-O correlation.

2.4. Properties of the $\text{In}_2\text{S}_3/\text{CIGSe}$ and $\text{In}_2(\text{O},\text{S})_3/\text{CIGSe}$ Interfaces

In Figure 3a, quantitative EBIC maps obtained at 10 kV are shown. Although in all three samples (rf- In_2S_3 @ RT, rf- In_2S_3 @ 220 °C, and rf- $\text{In}_2(\text{O}_{0.25}\text{S}_{0.75})_3$ @ 220 °C) a higher EBIC collection is observed at the position of the p-n junction, a clear difference in the magnitude of the collected EBIC current is registered. The lowest EBIC current in Figure 3b is observed for the rf- In_2S_3 @ RT sample, while the highest EBIC current is

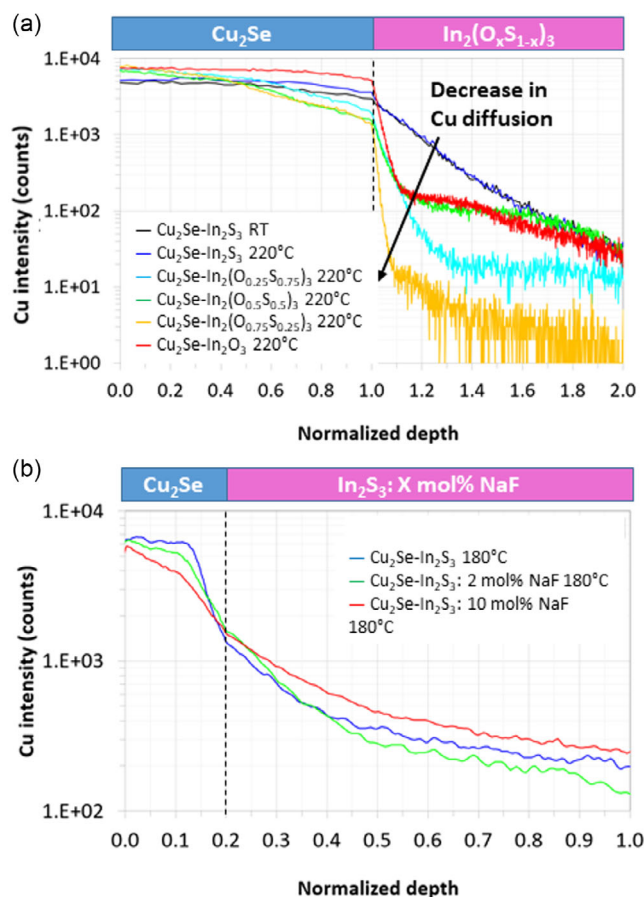


Figure 2. ToF-SIMS depth profiles performed with cesium cluster source showing the Cu signal for the $\text{Cu}_2\text{Se}-\text{In}_2(\text{O}_x\text{S}_{1-x})_3$ and $\text{Cu}_2\text{Se}-\text{In}_2\text{S}_3$: X mol% NaF model samples after annealing at 220 °C for 30 min. a) Study of the Cu diffusion from the Cu_2Se layer into the $\text{In}_2(\text{O}_x\text{S}_{1-x})_3$ layers with increasing oxygen content x sputtered at 220 °C. In addition, a second In_2S_3 sample sputtered at RT was added as reference. b) Study of Cu diffusion at 220 °C annealing temperature from the Cu_2Se layers into the In_2S_3 buffer layers which contain 0, 2, and 10 mol% NaF. All In_2S_3 : X layers were sputtered at 180 °C substrate temperature.

observed for rf- In_2S_3 @ 220 °C sample, for both acceleration voltages of 5 and 10 kV. The applied heat treatment of 220 °C to the In_2S_3 buffer layer leads to an improved p-n junction quality, and hence to a much higher current collection probability. However, when O is added to the In_2S_3 buffer the current collection probability is reduced. Interestingly, the same trend is observed for the open-circuit voltage V_{OC} depicted in Figure 3b.

The different In_2S_3 -based/ CIGSe heterointerfaces were investigated using high-resolution analytical techniques to better understand these differences in current collection probabilities among the samples. APT results presented in Figure 4, 5 prove the feasibility of exploring the composition of the In_2S_3 -based/ CIGSe heterointerface in 3D down to the sub-nanometer level, a requirement for the interface analysis. The elemental distribution in the 3D APT maps from Figure 4 highlights the presence of two types of internal interfaces, that is, of In_2S_3 -based/ CIGSe heterointerface and grain boundaries. Moreover, a distinct

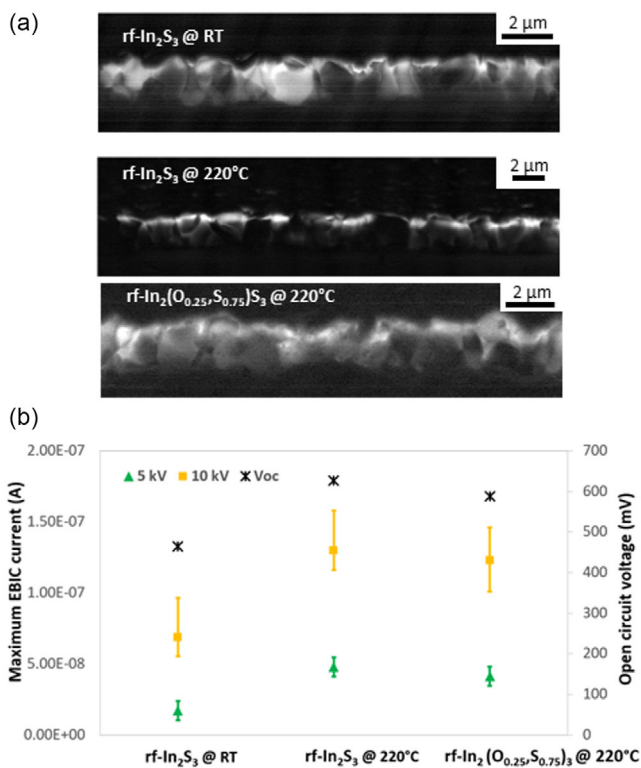


Figure 3. Quantitative EBIC results at the p–n junction of CIGSe solar cells with In₂S₃-based buffer layers. a) EBIC maps of CIGSe solar cells for the samples rf-In₂S₃ @ RT, rf-In₂S₃ @ 220 °C, and rf-In₂(O_{0.25}S_{0.75})₃ @ 220 °C obtained with an acceleration voltage of 10 kV. b) Corresponding maximum EBIC currents measured at the position of the p–n junction (with 5 and 10 kV) as well as the corresponding open-circuit voltage V_{OC} of the cells (from J – V data presented in Table S1, Supporting Information).

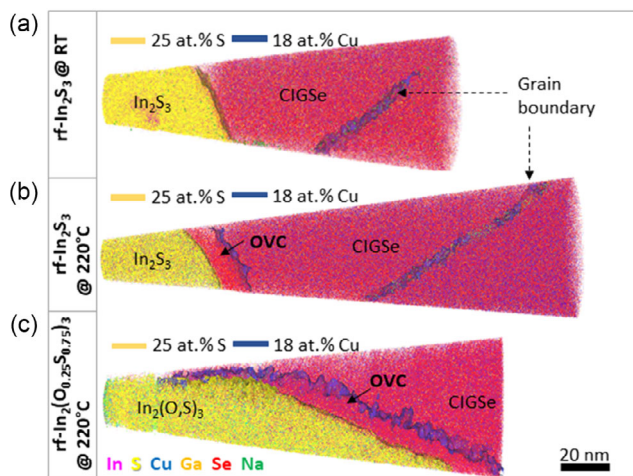


Figure 4. 3D APT maps of In₂S₃-based/CIGSe interface. 3D atomic distribution maps of In (pink), S (yellow), Cu (blue), Ga (kaki), Se (red), and Na (green). The 25 at% S isocomposition surface marks the location of the In₂S₃-based/CIGSe heterointerface, while the 18 at% Cu isocomposition surface marks the location of either grain boundaries in a,b) or a supplementary layer (OVC) found at the In₂S₃-based/CIGSe interface in b,c).

Cu-depleted layer is observed at the CIGSe–absorber surface for the two samples with rf-sputtered buffer at 220 °C (Figure 4b,c).

The APT composition analyses from Figure 5b,c suggest that this layer is a Cu-poor OVC, which is not present in the rf-In₂S₃ @ RT sample. It is important to mention here that this OVC layer shows a strong fluctuation in thickness (e.g., when comparing Figure 4b and Figure S3, Supporting Information). Moreover, in some regions this layer is completely absent which suggests that the OVC exists in spatially separated patches at the CIGSe surface in agreement with the work of Keller et al.^[37] Although it is important to point out here that the work of Keller et al.^[37] is done on Ag-containing CIGSe layers for which both the absorber surface and absorber/buffer interface exhibits completely different properties compared to the here studied Ag-free CIGSe cells.

The formation of this layer is promoted by the strong Cu diffusion from the CIGSe absorber toward the In₂S₃ buffer layer upon sputtering at 220 °C. Yet, this OVC layer is wider for the O-free In₂S₃ buffer layer (about 20 nm in rf-In₂S₃ @ 220 °C sample; see also the same Figure S3, Supporting Information where another region on the same rf-In₂S₃ @ 220 °C sample has been investigated) than the sample containing an O-alloyed buffer layer (about 5–7 nm in In₂(O_{0.25}S_{0.75})₃ @ 220 °C sample). This observation is explained by the stronger Cu diffusion from the CIGSe surface into the O-free In₂S₃ buffer layer than in the O-containing In₂S₃ buffer layer as shown in Figure 5b,c. Concerning the rf-In₂S₃ @ RT sample (Figure 5a), there is only a small gradient in the composition visible at the heterointerface, although 3 at% Cu is present inside the In₂S₃ buffer. This Cu diffusion at RT sputtering in the vicinity of the heterointerface can be explained by the plasma-induced moderate heat development during the sputtering process and/or the deposition conditions during the sputtering of the subsequent i-ZnO and ZnO:Al layers.

To further consolidate the OVC phase formation at the CIGSe surface, the structure of the buffer/CIGSe interface region was investigated by HRTEM imaging for the samples with buffer layers rf sputtered at 220 °C. **Figure 6A** shows a typical HRTEM image of the In₂S₃/CIGSe–interface region. The In₂S₃ layer exhibits locally a high degree of crystallinity, which is also confirmed by the Fourier transform (FT) (Figure 6Ab). In the imaged field of view, an in-plane orientation relationship between the lattice planes of In₂S₃ and CIGSe is observed, namely in the form of (31 $\bar{1}$)In₂S₃ || (31 $\bar{2}$) CIGSe. Thus, here In₂S₃ is epitaxially grown on CIGSe. Figure 6Ab–g presents experimental FTs and simulated diffraction patterns for comparison from different regions of Figure 6Aa. The FT in Figure 6Ab is calculated from the blue-dashed region of the In₂S₃ buffer. It agrees with the simulated diffraction pattern in [103]-zone axis for In₂S₃ with cubic crystal structure (space group $Fd\bar{3}m$, $a = 10.77$ Å, ICSD code 202 353^[38]) in Figure 6Ac. We note that reflections induced by double diffraction are included in the simulated diffraction patterns in addition to the kinematically allowed reflections. Figure 6Ad,e shows the FT of the red-dashed region in the CIGSe surface region in Figure 6Aa and the corresponding simulated diffraction pattern for CIGSe in [203]-zone axis (space group $I\bar{4}2d$, $a = b = 5.75$ Å, $c = 11.51$ Å, ICSD code 247 511.^[39]) The simulated diffraction pattern agrees with the

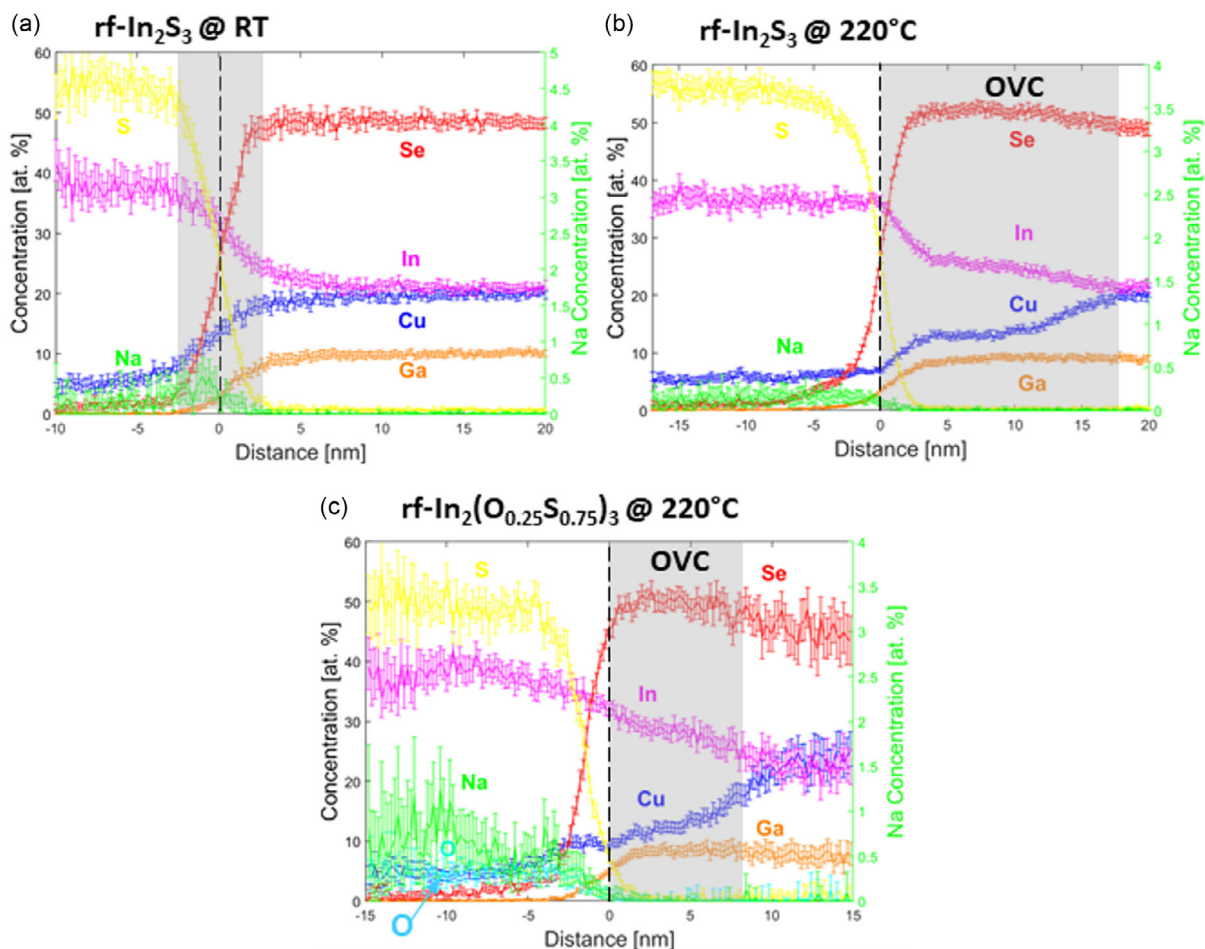


Figure 5. Composition profiles at the In_2S_3 -based/CIGSe heterointerface. These 1D proximity histograms are constructed from the 3D maps from Figure 4 using the 25 at% S isosurface. a) No Cu depletion is observed at the CIGSe surface, but rather a chemical intermixing at the In_2S_3 /CIGSe heterointerface (position 0), which is very often observed for thin layers deposited by sputtering. b,c) Yet, a strong Cu depletion is clearly observed at the CIGSe surface for the samples $\text{rf-In}_2\text{S}_3 @ 220^\circ\text{C}$ and $\text{rf-In}_2(\text{O}_{0.25}\text{S}_{0.75})_3 @ 220^\circ\text{C}$. This strong Cu depletion at the CIGSe surface (highlighted in gray) suggests the presence of an OVC layer.

experimental FT. However, two additional red-encircled superstructure reflections at half reciprocal lattice distances of the blue-encircled (020) and $(31\bar{2})$ reflections of CIGSe are observed in Figure 6Ad, which can be an indicator of the OVC phase. These superstructure reflections are typically observed in the region between In_2S_3 and CIGSe where the HRTEM image shows a slightly darker contrast (marked by white-dashed lines in Figure 6Aa). The experimental FT from CIGSe at a larger distance from the interface (white-dashed frame in Figure 6Aa) and simulated diffraction pattern in [203]-zone axis agrees well without showing superstructure reflections (Figure 6Af,g). Analyses by scanning transmission electron microscopy (STEM)/energy-dispersive X-ray spectroscopy (EDX) further substantiate the presence of the OVC phase because a reduction of Cu is observed in the CIGSe-surface region between the vertical black-dashed lines in Figure S2b, Supporting Information. In this region, the Se and Ga contents are unchanged compared to the CIGSe absorber while the In content increases, indicating Cu/In interdiffusion.

Figure 6B shows an HRTEM image of the $\text{In}_2(\text{O}_{0.25}\text{S}_{0.75})_3$ /CIGSe-interface region. In the imaged region, the $\text{In}_2(\text{O}_{0.25}\text{S}_{0.75})_3$ layer deposited on the $(\bar{1}12)$ planes of CIGSe has a nanocrystalline structure. This is independent of the orientation of the CIGSe grains since nanocrystalline $\text{In}_2(\text{O}_{0.25}\text{S}_{0.75})_3$ is also observable on other lattice-plane types. According to our previous experiments by nanobeam electron diffraction, the $\text{In}_2(\text{O}_{0.25}\text{S}_{0.75})_3$ layer consists of cubic In_2O_3 and tetragonal In_2S_3 nanocrystallites with a typical size of about 5 nm (see^[40] for details). The presence of disordered material between the nanocrystallites cannot be completely excluded. Superstructure reflections were not found in the $\text{In}_2(\text{O}_{0.25}\text{S}_{0.75})_3$ /CIGSe-interface region, but APT measurements (Figure 5) show that the thickness of the OVC layer is only 5–7 nm. It is therefore possible that the OVC phase cannot be detected by TEM due to the inclined interface with respect to the electron beam direction. In addition, a lower degree of ordering may weaken superstructure reflections. STEM/EDX analyses for this sample (Figure S2d, Supporting Information) show a slight Cu reduction

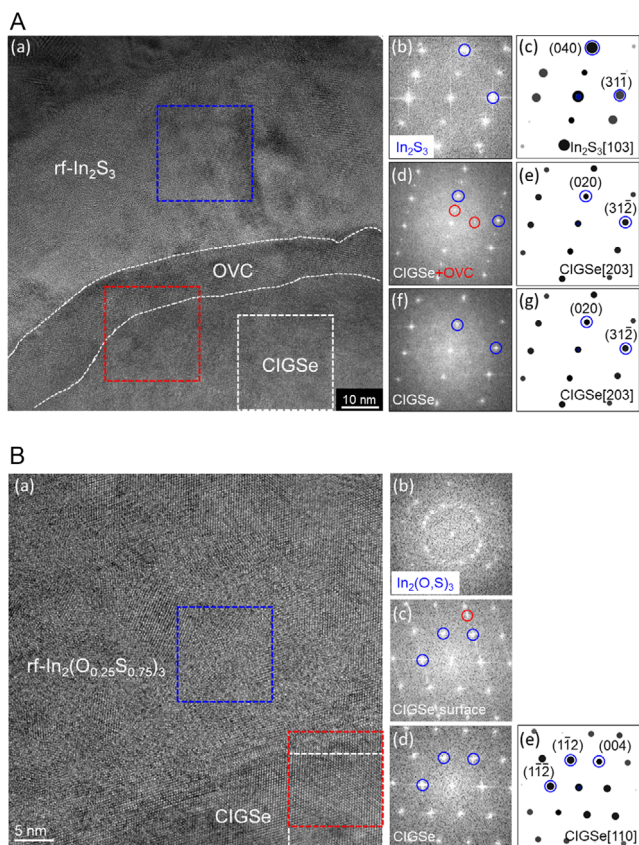


Figure 6. Structure of the A. In₂S₃/CIGSe and B. In₂(S_{0.75}O_{0.25})₃/CIGSe. A. a) Cross-section HRTEM image of the heterointerface region for the rf-In₂S₃ @ 220 °C. b,c) FT analysis of the rf-In₂S₃ and buffer from the blue-dashed frame in (a) with corresponding simulated diffraction pattern of In₂S₃ in [103]-zone axis (cubic In₂S₃ crystal structure: space group *Fd-3m*, *a* = 10.77 Å). The agreement between experimental FT and simulated diffraction pattern is highlighted by two blue-encircled reflections. d,e) FT analysis of the CIGSe-surface region from the red-dashed frame in (a) and simulated diffraction pattern of CIGSe in the [203]-zone axis (CIGSe crystal structure: space group *I-42d*, *a* = *b* = 5.75 Å, *c* = 11.51 Å). The red-marked superstructure reflections in (d) are missing in the simulated diffraction pattern indicating the presence of the OVC phase. This is in agreement with our previous work where OVC was identified at the surface of the CIGSe layer.^[42] f,g) FT analysis of the CIGSe absorber from the white-dashed square in (a) and simulated diffraction pattern of CIGSe in the [203]-zone axis. B. a) Cross-section HRTEM image of the In₂(S_{0.75}O_{0.25})₃/CIGSe-interface region. b) FT of the In₂(S_{0.75}O_{0.25})₃ buffer from the blue-dashed frame in (a). c) FT of the CIGSe surface region (red-dashed frame in (a)) with additional red-encircled reflection induced by the In₂(S_{0.75}O_{0.25})₃ buffer. d,e) FT of CIGSe in the white-dashed frame in (a) and simulated diffraction pattern for CIGSe in the [110]-zone axis (CIGSe crystal structure: space group *I-42d*, *a* = *b* = 5.75 Å, *c* = 11.51 Å). The agreement between FT and the simulated diffraction pattern is highlighted by the blue-encircled reflections.

close to the CIGSe surface between the vertical black-dashed lines. However, the gradients of the different elements across the interface are shallow due to the inclined orientation of the electron beam with respect to the interface and do not allow further conclusions on the element concentrations close to the CIGSe surface.

The formation of a relatively thick OVC layer for the sample with rf-sputtered In₂S₃ at 220 °C is supported by Raman spectra obtained at the CIGSe absorber surfaces after removing the sputtered In₂S₃-based buffers depicted in Figure S4, Supporting Information. Only the Raman spectrum of this sample exhibits a distinct signal around 155 cm⁻¹, which is attributed to OVC compounds like CuIn₃Se₅ or CuIn₅Se₈,^[41] whereas this feature is weak or absent for the samples with In₂S₃ sputtered at RT and In₂(O,S)₃ sputtered at 220 °C.

2.5. Role of the OVC Formation at the In₂(O_xS_{1-x})₃/CIGSe Interfaces

The present work indicates the formation of a 15–20 nm-thick OVC layer at the In₂S₃/CIGSe interface when the In₂S₃ is sputtered at 220 °C. This agrees with our previous studies done for the pure In₂S₃^[28] buffer or mixed In₂S₃-ZnS buffer^[42] as well as with refs. [43,44]. Such an OVC compound was absent when the surface of the CIGSe layer was sulfurized.^[45] Moreover, we demonstrate here that the presence of O in the In₂S₃ buffer impedes the Cu diffusion from the CIGSe surface into the In₂(O_xS_{1-x})₃ buffer reducing strongly the kinetics of the OVC layer formation and resulting in a much thinner OVC layer (of about 5 nm for In₂(O_{0.25}S_{0.75})₃ sputtered at 220 °C, but in some regions this layer was absent indicating strong fluctuations in thickness). Interestingly, the cell with thicker OVC layer is characterized by a higher V_{OC} value as well as a better current collection at the p–n junction (as shown by the EBIC investigations). Thus, this study implies that the presence of at least a 10 nm-thick OVC layer at the buffer/absorber interface is beneficial for cell performance; although a too-thick OVC layer might be detrimental for the solar cell. Regarding the optimum thickness of the OVC layer, no consensus was found until now given that Kwon et al.^[43] claimed that a 100 nm OVC layer is necessary, while Zheng et al.^[46] suggested that a 70 nm OVC layer is sufficient. Yet, we note here that a too-thick OVC layer can inhibit the carrier collection from the CIGSe bulk and, hence, deteriorate the cell performance.

Many previous theoretical works have claimed that such an OVC layer is present in the standard CIGSe cells containing a CdS buffer layer.^[46–48] This OVC layer can be easily doped by Cd from the CdS buffer resulting in an effective shift of the p–n junction from the CdS/CIGSe to OVC/CIGSe interface, reducing thus the charge recombination and leading to an increase in V_{OC} and thereby cell efficiency.^[48] Unfortunately, the formation of a distinct OVC layer at the CdS/CIGSe interface could not be validated experimentally, but rather the CIGSe surface was simply slightly depleted in Cu and enriched in Cd (almost 1:1 equivalence).^[49–53] Although the work from Kötschau et al.^[54] estimated a thickness of about 5–60 nm depending on the integral [Cu]/([Ga]+[In]) value of CIGSe absorbers by grazing-incidence X-ray diffraction, the APT near-atomic capabilities has proved that the thickness of this Cu-depleted region at the CIGSe surface is systematically only a few nanometers wide^[50,51] even when the cell was post-annealed at higher temperatures^[53] suggesting that only a few monolayers are Cu depleted and Cd enriched.

However, a distinct OVC layer is formed at the CIGSe surface in contact with In₂S₃-based buffer layers. This is because,

contrary to CdS (solubility limit of ≈ 10 ppm of Cu in CdS at 220 °C),^[55] the Cu solubility limit in In_2S_3 is much higher up to 5–9 at%^[56] favoring a strong Cu diffusion from the CIGSe surface into In_2S_3 . This is in agreement with our APT results where 4.4 at% Cu was detected in In_2S_3 , whereas no Cu was detected inside CdS.^[51] We note here that the detection limit in APT is about 10 ppm, so that means that the Cu content in CdS should be below 10 ppm in this case. Interestingly, the addition of O into In_2S_3 reduces the Cu solubility limit and, hence, it restrains the Cu diffusion inside $\text{In}_2(\text{O}_x\text{S}_{1-x})_3$ buffer as proved by APT and ToF-SIMS results explaining the formation of a much thinner OVC layer or even the absence of this phase in some regions of the cell.

The presence of an OVC layer at the buffer/absorber interface is assumed to be beneficial for device performance for various reasons. First, the OVC phase has shown a weak n-type character^[46] leading to a buried homojunction free of defects (no lattice mismatch) under extreme Cu-poor conditions. Second, the presence of the OVC layer lowers the valence band maximum as given in **Figure 7**, as predicted by theoretical calculations^[25,57] leading to a hole barrier toward the interface. It is well known that this hole barrier can have a benign effect on the performance of a CIGSe solar cell since it suppresses the charge recombination at the $\text{In}_2(\text{O}_x\text{S}_{1-x})_3/\text{CIGSe}$ interface. Simple device simulation using parameters as in Table 8.1 of ref. [58] have been performed in this work. Bandgap values and band offsets from refs. [25,45] have been used resulting in the band diagrams as depicted in **Figure 7**. Due to the negative conduction band offset at the CIGSe/ In_2S_3 interface device, simulation can easily reproduce the low $V_{\text{OC}} \approx 400$ mV for the cell without OVC as was observed in the experiment. The corresponding band diagram is depicted in **Figure 7a**. The introduction of an OVC layer of 20 nm thickness in the device model (see **Figure 7b**) increases the V_{oc} to 610 mV. We note here that

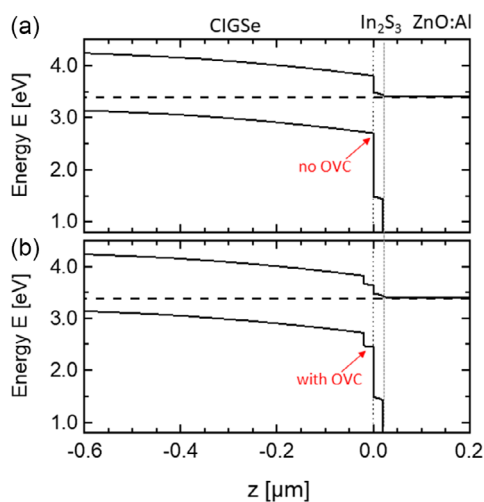


Figure 7. Band diagrams from AforsHet simulations at the CIGSe/ In_2S_3 interface for the cell a) without OVC and b) with OVC. These simulations indicate that the presence of the 20 nm-thick OVC at the heterointerface lowers the valence band edge at the surface of the absorber and hence reduces interface recombination and increases V_{OC} . The employed parameters are given in the Section D, Supporting Information.

these V_{OC} values (obtained by employing AforsHet simulations) are very close to the experimental values shown in **Figure 1** and listed in Table S1, Supporting Information that is, 465 mV for the cell without OVC (rf- In_2S_3 @ RT sample) and 627 mV for the cell with OVC (rf- In_2S_3 @ 220 °C sample). The reason for the efficiency increase upon OVC formation is the reduced hole density at the interface to the buffer layer, here In_2S_3 . This OVC layer thus would reduce the deleterious impact of the unfavorable band alignment between CIGSe and In_2S_3 . If the OVC layer becomes too thin as in the case of the $\text{In}_2(\text{O}_x\text{S}_{1-x})_3$ buffer, local spots of interface recombination may become active which results in a combination of interface and bulk recombination. This may reduce the V_{OC} as observed for the rf- $\text{In}_2(\text{O}_{0.25}\text{S}_{0.75})_3$ @ 220 °C sample. In case the OVC is too thick and in combination with a buffer a secondary barrier can be formed, partially inhibiting the photogenerated carrier transport and thus creating a kink and FF decrease as observed for the cell with the pronounced OVC (rf- In_2S_3 @ 220 °C sample).

Moreover, the formation of the OVC thin layer at the surface of CIGSe will not only reduce the VBM as explained above, but also will lower the CBM as proved by Ghorbani et al.^[25] and in agreement with our simulation from **Figure 7b**.

3. Conclusion

In this work, we investigate the buffer/CIGSe absorber interface for a series of sputter-deposited In_2S_3 buffers with and without O. We find that the solar cell with the highest open-circuit voltage value is obtained for the O-free In_2S_3 buffer sputtered at 220 °C. For this sample, a 20 nm-thick OVC is detected at the absorber surface by APT, HRTEM analyses, and Raman. A much thinner OVC layer (5 nm) or even the absence of this layer was found for the cell with $\text{In}_2(\text{O}_{0.25}\text{S}_{0.75})_3$ buffer layer where O was inserted. The volume fraction of this OVC is directly linked with the magnitude of Cu diffusion from the CIGSe absorber surface inside the $\text{In}_2(\text{O}_x\text{S}_{1-x})_3$ buffer. The O addition reduces strongly the Cu diffusion inside the buffer layer until complete suppression for very high O contents in the buffer in agreement with the ToF-SIMS diffusion experiments on the $\text{Cu}_2\text{Se}-\text{In}_2(\text{O},\text{S})_3$ samples. Based on the AforsHet simulations, we discussed that the presence of the OVC layer may lower the valence band maximum, leading to a hole barrier and suppressing the charge carrier recombination at the $\text{In}_2(\text{O}_x\text{S}_{1-x})_3/\text{CIGSe}$ interface. This may explain the increase in the open-circuit voltage observed when a 20 nm-thick OVC layer is present at the heterointerface.

4. Experimental Section

Sample Growth: CIGSe thin-film solar cells were prepared with an in-line multistage coevaporation process on Mo-coated soda-lime glass.^[59] The CIGSe layers exhibited a thickness of around 2.3 μm with $[\text{Ga}]/([\text{Ga}]+[\text{In}])$ and $[\text{Cu}]/([\text{Ga}]+[\text{In}])$ ratios of about 0.3 and 0.8, respectively, as determined by X-Ray fluorescence measurement. The CIGSe layers contained Na and partially K through alkali diffusion from the soda-lime glass substrate. No additional heavy alkali postdeposition treatment^[60] (like Rb or Cs) was applied after the CIGSe process. Subsequently, rf-sputtered $\text{In}_2(\text{O}_x\text{S}_{1-x})_3$ buffers with different oxygen contents, rf-sputtered i-ZnO as a high-resistive layer, and dc-sputtered ZnO:Al as front contact were deposited (similar to the work in ref. [25]). The cells were completed with

Ni/Al/Ni grid fingers and the total cell area was 0.5 cm². All cells featured no antireflective coating.

The In₂(O_xS_{1-x})₃ buffer layers were rf magnetron sputtered at RT or at 220 °C after CIGSe deposition in a VON ARDENNE (Dresden, Germany) high-vacuum sputtering system of type CS 730S. Commercially available ceramic In₂(O_xS_{1-x})₃ (x = 0, 0.25) targets with a diameter of 20 cm^[25,31,61] were employed. No O was added to the sputtering gas, consisting of pure Ar, so that the layer composition nearly corresponded to the target composition. As a reference buffer layer, we applied solution-grown CdS with a thickness of around 50 nm as deposited from a thiourea-based process with a bath temperature of 65 °C.

In addition to the fabrication of complete CIGSe solar cells, various In₂(O,S)₃-based layers on glass substrates, namely, In₂(O_xS_{1-x})₃ with x = 0, 0.25, 0.50, 0.75, and 1 sputtered at 220 °C (for x = 0 an additional layer was sputtered at RT) from commercially available ceramic targets as well as In₂S₃: X mol% NaF (with X = 0, 2, and 10) sputtered at 180 °C with sputtered Cu₂Se on the top were prepared as model samples to study temperature-induced Cu interdiffusion which may occur at the buffer/CIGSe interface. These Cu₂Se-In₂(O_xS_{1-x})₃ and Cu₂Se-In₂S₃: X mol% NaF model samples were annealed at 220 °C for 30 min and consisted of the following stacking sequence (from top to bottom): sputtered Cu₂Se/In₂(O,S)₃ based layer (without or with Na)/glass substrate.

Methods: Current density–voltage (*J*–*V*) measurements were performed with a WACOM (Saitama, Japan) AM1.5G solar simulator with four-point geometry at standard testing conditions with a silicon reference solar cell for calibration.

Temperature-dependent *J*–*V* measurements were conducted in a liquid-nitrogen-cooled cryostat with a Xe lamp illumination.

ToF-SIMS measurements were carried out with a ToF5-SIMS instrument from IONTOF. The analyzing Bi⁺-ion beam was run at 30 keV and probed over an area of 50 × 50 μm². Furthermore, a Cs-ion gun with 2 keV and a rasterized area of 500 × 500 μm² was used to reach good sputter rates.

Raman spectroscopic analysis was conducted on the thin films utilizing a 532 nm frequency-doubled Nd:YAG laser installed in the WITec alpha300R confocal microscope. The measurements were carried out with a 100× objective in ambient conditions. To prevent laser-induced damage and obtain higher Raman signals, the laser power was optimized to obtain the best results at 0.5 mW. A grating with 1800 lines per millimeter allowed for a resolution of ≈1 cm⁻¹. Same acquisition conditions were used for all the samples for better comparison. Multiple spots were measured to ensure the representativeness and homogeneity of the sample. For the laser parameters used here, an estimated analyzed depth range by Raman was about 150–350 nm in CIGSe thin film.

The EBIC measurements were carried out on freshly cleaved cross sections (not polished) at acceleration voltages of 5 and 10 kV under low-electron beam currents to avoid high-injection regime. The transfer of samples for EBIC measurements was immediate after cleavage to avoid surface oxidation. A smart EBIC holder by Gatan Inc. was used for EBIC data acquisition and analysis in the dual-beam Nanolab Thermo Fisher setup. All EBIC measurements were performed in the dark without any external bias at room temperature. A gain of 5 × 10⁵ and a dwell time of 40 μs was used for quantitative data acquisition.

The preparation of the APT specimens was done using the standard “lift-out method”.^[62] This is a very well-established method that involves the dual-beam scanning electron microscope (SEM) and focused ion beam (FIB) within the Helios Nanolab Thermo Fisher system.^[62] Limitations in terms of sample preparation using FIB were discussed in our previous works.^[53,63] We mention here that all these limitations (amorphization and stoichiometry modifications) can be completely suppressed by performing a final low-kV cleaning at very low-voltage and -current conditions for these needle-shaped specimens. Moreover, the usage of a protection layer deposited on the surface of the specimen before starting with the FIB preparation method can help further in achieving Ga-free specimens. The APT measurements were performed with the LEAP 4000X Si system from Cameca, Ametek, at a temperature of 40 K (cryogenic temperature), to avoid the migration of atoms to the surface of the needle-shaped specimen. The UV laser pulses with the wavelength

of 355 nm and the laser energy of 3 pJ were applied to the tip. Moreover, the pulse frequency used was 250 kHz and the evaporation rate was 0.5%.

TEM was applied to characterize the structural properties and micro-chemistry of the buffer/absorber interfaces. For this purpose, cross-sectional TEM samples were prepared by Ga⁺-FIB milling in a Thermo Fisher Helios G4FX dual-beam microscope using the lift-out technique. Si lift-out grids were used instead of Cu lift-out grids to avoid artifacts in the quantification of the Cu content in CIGSe. FIB lamellae were first thinned at 30 kV and finally polished by a Ga⁺-ion beam with a low accelerating voltage of 1 kV to minimize material damage. Further details on the TEM specimen preparation were described by Jin et al.^[64] HRTEM imaging was performed with an image aberration-corrected FEI Titan³ 80–300 transmission electron microscope at 300 kV. Chemical analyses by EDX were performed in the STEM mode with a FEI Tecnai Osiris operated at 200 kV. For EDX analyses, the microscope was equipped with a Super-X system comprising four silicon drift detectors. X-ray maps were recorded in the so-called HyperMap mode via the Bruker software Esprit version 1.9. Subsequently, quantification of the raw EDX data was carried out by the Bruker Esprit software (version 2.1) using calculated *k*-factors in the thin-film approximation and implemented elemental mass absorption coefficients to consider X-ray absorption (for further, details see Jin et al.^[64]). Element-line profiles were obtained from the quantified EDX data.

Device simulations were performed using the software Aforshet with input parameters as listed in Section D, Supporting Information. These simulations helped to model the p–n heterojunction between the In₂(O_xS_{1-x})₃ buffer and CIGSe absorber. Based on these simulations the V_{OC} values could also be estimated and compared with the experimental values.

Supporting Information

Supporting Information is available from the Wiley Online Library or from the author.

Acknowledgements

This work received funding from the German Federal Ministry for Economic Affairs and Climate Action (BMWK) within the EFFCIS (contract numbers 0324076A, 0324076C, 0324076E, and 0324076F) and EFFCIS-II (contract numbers 03EE1059A, 03EE1059C, 03EE1059E, and 03EE1059F) projects.

Conflict of Interest

The authors declare no conflict of interest.

Author Contributions

Oana Cojocaru-Mirédin: Conceptualization (lead); Data curation (equal); Funding acquisition (lead); Investigation (equal); Methodology (lead); Project administration (lead); Supervision (lead); Validation (lead); Writing—original draft (lead). **Dimitrios Harikos:** Data curation (supporting); Funding acquisition (supporting); Writing—original draft (equal). **Wolfram Hempel:** Data curation (supporting). **Ana Kanevce:** Data curation (supporting); Formal analysis (supporting). **Xiaowei Jin:** Data curation (supporting); Formal analysis (supporting); Writing—original draft (supporting). **Jens Keutgen:** Data curation (supporting). **Mohit Raghuvanshi:** Data curation (supporting). **Reinhard Schneider:** Data curation (supporting); Writing—original draft (supporting). **Roland Scheer:** Data curation (supporting); Writing—original draft (supporting). **Dagmar Gerthsen:** Data curation (supporting); Formal analysis (supporting); Funding acquisition (supporting); Writing—original draft (supporting). **Wolfram Witte:**

Conceptualization (equal); Data curation (supporting); Formal analysis (supporting); Funding acquisition (equal); Writing—original draft (equal).

Data Availability Statement

The data that support the findings of this study are available from the corresponding author upon reasonable request.

Keywords

atom probe tomography, CIGSe solar cells, nanocharacterization, ordered vacancy compound

Received: August 4, 2024

Revised: October 28, 2024

Published online: November 24, 2024

- [1] H. Moualkia, S. Hariach, M. S. Aida, *Thin Solid Films* **2009**, 518, 1259.
- [2] M. F. Rahman, J. Hossain, A. Kuddus, S. Tabassum, M. H. K. Rubel, H. Shirai, A. B. M. Ismail, *Appl. Phys. A* **2020**, 126, 145.
- [3] F. A. Jhuma, M. Z. Shaily, M. J. Rashid, *Mater. Renewable Sustainable Energy* **2019**, 8, 6.
- [4] S. Spiering, A. Eicke, D. Hariskos, M. Powalla, N. Naghavi, D. Lincot, *Thin Solid Films* **2004**, 451, 562.
- [5] C. H. Fischer, N. A. Allsop, S. E. Gledhill, T. Köhler, M. Krüger, R. Sáez-Araoz, Y. Fu, R. Schwieger, J. Richter, P. Wohlfart, P. Bartsch, N. Lichtenberg, M. C. Lux-Steiner, *Sol. Energy Mater. Sol. Cells* **2011**, 95, 1518.
- [6] M. A. Mughal, R. Engelken, R. Sharma, *Sol. Energy* **2015**, 120, 131.
- [7] P. Soni, M. Raghuvanshi, R. Wuerz, B. Berghoff, J. Knoch, D. Raabe, O. Cojocaru-Mirédin, *Energy Sci. Eng.* **2019**, 7, 478.
- [8] M. M. Islam, S. Ishizuka, A. Yamada, K. Sakurai, S. Niki, T. Sakurai, K. Akimoto, *Sol. Energy Mater. Sol. Cells* **2009**, 93, 970.
- [9] T. Nakada, M. Mizutani, *Jpn. J. Appl. Phys.* **2002**, 41, L165.
- [10] S. Merdes, V. Malinen, F. Ziem, I. Laueremann, M. Schüle, F. Stober, F. Hergert, N. Papathanasiou, R. Schlattmann, *Sol. Energy Mater. Sol. Cells* **2014**, 126, 120.
- [11] M. Zutter, J. Virtuoso, P. Anacleto, L. Yasin, M. Alves, M. Madeira, O. Bondarchuk, S. Mitra, D. Fuster Signes, J. M. Garcia, F. Briones, R. Waechter, O. Kiowski, D. Hariskos, D. Colombara, S. Sadewasser, *Phys. Status Solidi RRL* **2019**, 13, 1900145.
- [12] S. Hwang, L. Larina, H. Lee, S. Kim, K. S. Choi, C. Jeon, B. T. Ahn, B. Shin, *ACS Appl. Mater. Interfaces* **2018**, 10, 20920.
- [13] P. M. P. Salomé, J. Keller, T. Törndahl, J. P. Teixeira, N. Nicoara, R.-R. Andrade, D. G. Stroppa, J. C. González, M. Edoff, J. P. Leitão, S. Sadewasser, *Sol. Energy Mater. Sol. Cells* **2017**, 159, 272.
- [14] J. Chantana, T. Kato, H. Sugimoto, T. Minemoto, *ACS Appl. Mater. Interfaces* **2018**, 10, 11361.
- [15] S. Song, D. B. Khadka, S. Y. Kim, J. H. Kim, J. Gwak, J. H. Yun, K. Yoon, *Curr. Appl. Phys.* **2014**, 14, S17.
- [16] T. A. Byung, L. Larina, H. K. Ki, J. A. Soong, *Pure Appl. Chem.* **2008**, 80, 2091.
- [17] M. Nakamura, Y. Kouji, Y. Chiba, H. Hakuma, T. Kobayashi, T. Nakada, in *2013 IEEE 39th Photovoltaic Specialists Conf. (PVSC)*, Tampa, Florida **2013**.
- [18] A. Hultqvist, J. Keller, N. M. Martin, F. Larsson, T. Törndahl, *ACS Appl. Energy Mater.* **2023**, 6, 9824.
- [19] F. Larsson, J. Keller, J. Olsson, O. Donzel-Gargand, N. M. Martin, M. Edoff, T. Törndahl, *Sol. Energy Mater. Sol. Cells* **2020**, 215, 110647.
- [20] T. Jawinski, C. Sturm, R. Clausing, H. Kempa, M. Grundmann, R. Scheer, H. Von Wenckstern, *AIP Adv.* **2022**, 12, 125215.
- [21] W. Rehwald, G. Harbeke, *J. Phys. Chem. Solids* **1965**, 26, 1309.
- [22] X. He, P. Ercius, J. Varley, J. Bailey, G. Zapalac, T. Nagle, D. Poplavskyy, N. Mackie, A. Bayman, V. Lordi, A. Rockett, *Prog. Photovoltaics Res. Appl.* **2019**, 27, 255.
- [23] B. K. Meyer, A. Polity, B. Farangis, Y. He, D. Hasselkamp, Th. Krämer, C. Wang, *Appl. Phys. Lett.* **2004**, 85, 4929.
- [24] L. Larina, K. H. Kim, K. H. Yoon, M. Konagai, B. T. Ahn, *J. Electrochem. Soc.* **2004**, 151, C789.
- [25] E. Ghorbani, X. Jin, D. Perera, R. Schneider, D. Gerthsen, D. Hariskos, R. Menner, W. Witte, K. Albe, *J. Appl. Phys.* **2024**, 135, 73101.
- [26] E. Niemi, J. Sterner, P. Carlsson, J. Oliv, E. Jaremalm, S. Lindström, in *31st European Photovoltaics Solar Energy Conf. Exhibition*, Hamburg, Germany **2015**.
- [27] N. Barreau, J. C. Bernède, H. E. Maliki, S. Marsillac, X. Castel, J. Pinel, *Solid State Commun.* **2002**, 122, 445.
- [28] P. Soni, M. Raghuvanshi, R. Wuerz, B. Berghoff, J. Knoch, D. Raabe, O. Cojocaru-Mirédin, *Sol. Energy Mater. Sol. Cells* **2019**, 195, 367.
- [29] P. Soni, O. Cojocaru-Miredin, D. Raabe, in *2015 IEEE 42nd Photovoltaic Specialists Conf. PVSC 2015*, New Orleans **2015**.
- [30] W. Witte, W. Hempel, S. Paetel, R. Menner, D. Hariskos, *ECS J. Solid State Sci. Technol.* **2021**, 10, 55006.
- [31] D. Hariskos, W. Hempel, R. Menner, W. Witte, *Appl. Sci.* **2020**, 10, 1052.
- [32] H. Wilhelm, H.-W. Schock, R. Scheer, *J. Appl. Phys.* **2011**, 109, 84514.
- [33] R. Scheer, *J. Appl. Phys.* **2009**, 105, 104505.
- [34] L. Kronik, D. Cahen, H. W. Schock, *Adv. Mater.* **1998**, 10, 31.
- [35] D. H. Buckley, NASA TN D-7340, **1973**.
- [36] P. Pistor, N. Allsop, W. Braun, R. Caballero, C. Camus, C.-H. Fischer, M. Gorgoi, A. Grimm, B. Johnson, T. Kropp, I. Laueremann, S. Lehmann, H. Mönig, S. Schorr, A. Weber, R. Klenk, *Phys. Status Solidi A* **2009**, 206, 1059.
- [37] J. Keller, L. Stolt, K. V. Sopiha, J. K. Larsen, L. Riekehr, M. Edoff, *Sol. RRL* **2020**, 4, 2000508.
- [38] C. Adenis, J. Olivier-Fourcade, J.-C. Jumas, E. Philippot, *Rev. Chim. Miner.* **1987**, 24, 10.
- [39] M. Souilah, A. Lafond, C. Guillot-Deudon, S. Harel, M. Evain, *J. Solid State Chem.* **2010**, 183, 2274.
- [40] X. Jin, R. Schneider, R. Popescu, D. Hariskos, W. Witte, M. Powalla, D. Gerthsen, *Semicond. Sci. Technol.* **2020**, 35, 34001.
- [41] C. Rincón, S. M. Wasim, G. Marín, J. M. Delgado, J. R. Huntzinger, A. Zwick, J. Galibert, *Appl. Phys. Lett.* **1998**, 73, 441.
- [42] O. Cojocaru-Mirédin, Y. Fu, A. Kostka, R. Sáez-Araoz, A. Beyer, N. Knaub, K. Volz, C.-H. Fischer, D. Raabe, *Prog. Photovoltaics: Res. Appl.* **2015**, 23, 705.
- [43] S. H. Kwon, S. C. Park, B. T. Ahn, K. H. Yoon, J. Song, *Sol. Energy* **1998**, 64, 55.
- [44] D. Abou-Ras, Doctoral Thesis, ETH Zurich, **2005**.
- [45] O. Cojocaru-Mirédin, E. Ghorbani, M. Raghuvanshi, X. Jin, D. Pandav, J. Keutgen, R. Schneider, D. Sáez-Araoz, K. Albe, R. Scheer, *Nano Energy* **2021**, 89, 106375.
- [46] X. Zheng, W. Li, A. G. Aberle, S. Venkataraj, *Curr. Appl. Phys.* **2016**, 16, 1334.
- [47] D. Schmid, M. Ruckh, F. Grunwald, H. W. Schock, *J. Appl. Phys.* **1993**, 73, 2902.
- [48] A. Sharan, F. P. Sabino, A. Janotti, N. Gaillard, T. Ogitsu, J. B. Varley, *J. Appl. Phys.* **2020**, 127, 65303.
- [49] Z. Li, X. Yu-Ming, X. Chuan-Ming, H. Qing, L. F. Fang, L. Chang-Jian, S. Yun, *Thin Solid Films* **2012**, 520, 2873.
- [50] O. Cojocaru-Mirédin, P. Choi, R. Wuerz, D. Raabe, *Appl. Phys. Lett.* **2011**, 98, 103504.
- [51] O. Cojocaru-Mirédin, P. Choi, R. Wuerz, D. Raabe, *Appl. Phys. Lett.* **2012**, 101, 181603.

- [52] A. Koprek, O. Cojocaru-Miredin, R. Wuerz, C. Freysoldt, B. Gault, D. Raabe, *IEEE J. Photovoltaics* **2017**, *7*, 313.
- [53] A. Koprek, P. Zabierowski, M. Pawlowski, L. Sharma, C. Freysoldt, B. Gault, R. Wuerz, O. Cojocaru-Mirédin, *Sol. Energy Mater. Sol. Cells* **2021**, *224*, 110989.
- [54] I. M. Kötschau, H. W. Schock, *J. Phys. Chem. Solids* **2003**, *64*, 1559.
- [55] G. A. Sullivan, *Phys. Rev.* **1969**, *184*, 796.
- [56] P. Pistor, Doctoral Thesis, FU Berlin, **2009**.
- [57] M. Gloeckler, J. R. Sites, *Thin Solid Films* **2005**, *480–481*, 241.
- [58] R. Scheer, H. Schock, in *Chalcogenide Photovoltaics*, Wiley, Weinheim, Germany, **2011**.
- [59] R. Gutzler, W. Witte, A. Kanevce, D. Hariskos, S. Paetel, *Prog. Photovoltaics: Res. Appl.* **2023**, *31*, 1023.
- [60] P. Jackson, R. Wuerz, D. Hariskos, E. Lotter, W. Witte, M. Powalla, *Phys. Status Solidi RRL* **2016**, *10*, 583.
- [61] M. Powalla, B. Dimmler, R. Schaeffler, G. Voorwinden, U. Stein, H. D. Mohring, F. Kessler, D. Hariskos, in *Proc. of the 19th European Photovoltaic Solar Energy Conf.*, Freiburg, Germany **2004**.
- [62] K. Thompson, D. Lawrence, D. J. Larson, J. D. Olson, T. F. Kelly, B. Gorman, *Ultramicroscopy* **2007**, *107*, 131.
- [63] O. Cojocaru-Mirédin, T. Schwarz, D. Abou-Ras, *Scr. Mater.* **2018**, *148*, 106.
- [64] X. Jin, R. Schneider, E. Müller, M. Falke, R. Terborg, D. Hariskos, A. Bauer, W. Witte, M. Powalla, D. Gerthsen, *Microsc. Microanal.* **2023**, *29*, 69.